Research On Twin Tungsten Electrode – Wire Electrode Indirect Arc Additive Manufacturing Process

Yanli Zhu[1*], Haibo Liu[1], Peimin Li[1], Dianguo Ma[1], Junyu Zhang[1], Guangsheng Lv[1], Hongjie Fang[1], Qingyun Yang[1], and Lincai Zhang[1*]

[1] *School of Mechanical and Electrical Engineering, Zaozhuang University, Zaozhuang, 277160, China*
[*] *Corresponding author. E-mail: zhuyanli007@163.com (Y. Zhu); vicande@hotmail.com (L. Zhang)*

Received: April 3, 2026; Accepted: June. 04, 2026

The low forming efficiency and high heat accumulation existed in TIG additive manufacturing process hinder its further development and application. A novel twin tungsten electrode – wire electrode indirect arc (TTWIA) additive manufacturing has great potential to solve the above problem due to its high wire deposition rate and lower heat input. Different from TIG, the substrate heat input of TTWIA excluded the heat production in the electrode region and the resistive heating, and the wire melting heat of TTWIA was predominantly composed of the heat production in the electrode region. Consequently, the molten pool temperature of TTWIA was relatively lower, and the wire deposition rate of TTWIA was more than 2.75 times higher than that of conventional TIG under the identical experimental conditions. Moreover, the surface roughness and material utilization rate of the component fabricated by TTWIA could reach 1.21 mm and 83.74%, respectively. Additionally, the top and bottom regions of the component fabricated by TTWIA featured coarse columnar grains, while the middle region showed fine equiaxed grains. Furthermore, the tensile strength and elongation of the component approached those of original wire, and possessed significant anisotropy.

Keywords: Wire and arc additive manufacturing, TTWIA, Wire deposition rate, Arc shape, Droplet transfer, Forming

http://dx.doi.org/10.6180/jase.202611_34.053

1. Introduction

Wire and arc additive manufacturing (WAAM) is being valued by more and more researchers because of its advantages of high productivity, high material utilization, and low cost [1]. Generally, heat sources used for WAAM included tungsten inert gas (TIG), gas metal arc (GMA), and plasma arc (PA) [2]. However, the deposition efficiency and forming quality of conventional WAAM processes struggle to meet the production demands of modern industry. To achieve high-quality and high efficiency WAAM, researchers have conducted extensive studies on WAAM processes, continuously developing novel WAAM techniques.

In twin-electrode TIG based additive manufacturing, the power-function-curve model and tangent overlapping model were proposed, which could precisely forecast the bead overlapping behavior, with a maximum deviation not exceeding 6% [3]. During three-electrode TIG welding, a more stable and centralized arc was achieved under the conditions of a distance smaller than 5 mm between the electrodes, and with the electrode angle and torch angle at 40° and 20°, respectively [4]. Moreover, a hot-wire tungsten inert gas arc (HWTIG) was employed to prototype Inconel 625 alloy component, and the ultimate tensile strengths in the direction perpendicular and parallel to the deposited layer separately achieved 599 MPa and 713 MPa, which presented apparently anisotropic property [5]. However, molten pool was still the primary heat source for wire melting, which suggested that the molten pool with a larger volume would be desired to achieve a higher wire deposition rate. Therefore, efficient additive manufacturing process was on the premise of high arc energy. Excessive heat accumulation during WAAM can induce various defects, including collapse [6], high residual stress and distortion [7], crack [8], coarse columnar grain [9], and porosity [10], which remarkably compromise the accuracy and performance of the forming components.

To overcome the high heat input, an additive manufacturing technology based STWIA was proposed, in which the low process temperature and high cooling rate were achieved, without sacrificing the forming efficiency of the deposited component [11, 12]. Moreover, to improve the wettability and spreading of the STWIA's molten pool, a twin tungsten electrode – wire electrode indirect arc (TTWIA) was proposed by the authors, where the arc shape and droplet transfer behaviour of TTWIA were pronouncedly affected by wire feeding speed and arc current [13–15]. Additionally, TTWIA was firstly applied to additive manufacturing, and the forming characteristic was preliminarily investigated [16, 17]. However, the thermal process of TTWIA has not been systematically studied, and the law and mechanism of the heat and mass transfer of TTWIA remain unclear.

In this paper, a comparative study between TIG and TTWIA additive manufacturing processes was carried out. To reveal the heat and mass transfer mechanism of TTWIA, the arc shape, droplet transfer behavior, molten pool temperature field, and forming appearance of TTWIA additive manufacturing were observed and measured, as well as establishing the corresponding physical models.

2. Experiment method

Fig. 1 shows the experimental setup of additive manufacturing based TTWIA. Two TIG welding torches were separately linked to the negative poles of two welding powers (AOTAI WSME-315), whereas the welding wire was linked to the positive pole of two welding powers. Notably, nothing was connected to substrate. Therefore, two circuits were built among the three electrodes, which induced the indirect arc burnt at the ends of the above electrodes. A thin-walled part was built layer by layer in a single travel direction, namely the wire was in front, followed by the two tungsten electrodes. Besides, a dwell time of nearly 60 s was also set between the neighbouring layers. As listed in Table 1, a Q235 mild steel plate with 15 mm thickness and a Ø1.2 mm welding wire (AWS ER70S-6) were employed as the substrate and the filler wire, respectively. Besides, the detailed deposition parameters are listed in Table 2.

In the imaging system, an infrared camera equipment was utilized to measure the molten pool temperature distribution. The specification of the infrared camera (SAT G95) were 384 × 288 pixel resolution, 8~14 μm spectral range, and 50 Hz sampling frequency respectively. Moreover, a 60° was set between the infrared camera and the deposited bead aimed to eliminate the interference of the welding torch on molten pool temperature acquisition. Additionally, a high-speed camera (Mega-speed MS50K) was used to collect arc morphology and droplet transfer process, during which a 500 mm spacing between the camera and arc was set. In the sensing system, the voltage of TTWIA was considered as the average of the voltage values collected by two voltage sensors, because both power sources had same type and parameter, together with parallel circuit. Additionally, the current of TTWIA was equal to the sum of the current values collected by two Hall current sensors.

Table 1. Chemical composition of the workpiece and the wire (wt. %).

	C	Mn	Si	S	P	Fe
Q235	0.15	0.50	0.20	0.03	0.03	Re
ER70S-6	0.078	1.45	0.87	0.013	0.012	Re

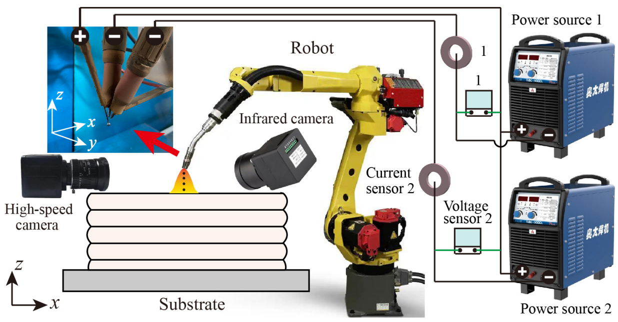

Fig. 1. Integral frame of experimental setup.

Fig. 2(a) shows the sample positions used for capturing microstructure, along with measuring microhardness and tensile strength. Wire cutting machine was employed to cut these samples from the thin-walled part. The metallographic samples were coarsely and finely ground by sandpaper, followed by roughly and finely polished by diamond paste. The samples were corroded by 96% ethanol + 4% nitric acid solution for 15 s. The microstructure was observed by optical microscopy (OM). Microhardness was measured using a TouchHV-1000A Vickers tester along the midline in cross section of the sample from bottom to top, in which the load and loading time were separately set to 500 g and 10 s. The tensile experiment was carried out via a

SDS100 tensile laboratory instrument, in which the loading rate was set to 1 mm/min in accordance with Chinese

Table 2. Deposition parameter.

Method	Arc current (A)	Wire feeding velocity (m/min)	Deposition velocity (mm/s)	Total layers	Dwell time (s)	Tungsten tip height (mm)
TTWIA	200	6.75	5	10	60	5
TIG	200	1.80	5	10	60	5

standard GB/T 228.1-2021. The small size of the tensile sample was selected and displayed in Fig. 2(b), owing to the dimension of the components [18, 19]. Notably, the average of the three tensile samples was taken as the resultant tensile strength.

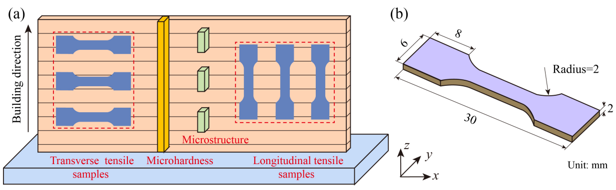

Fig. 2. (a) Selected specimen location; (b) Tensile specimen geometry size.

3. Results and discussion

3.1. Arc shape and droplet transfer

The typical arc shape and droplet transfer behavior of TTWIA were presented in Fig. 3. For TTWIA with a specific current, when matched with an appropriate wire feeding speed, it remained stable and extended freely during combustion. Along the direction parallel to the twin tungsten electrodes arrangement, the arc assumed a broom-shaped morphology (Fig. 3(b)), while along the perpendicular direction, it exhibited a conical configuration (Fig. 3(e)). The closer to the electrode tip, the higher the arc brightness and temperature. As shown in Fig. 4(a, b), owing to the special electrode structure of TTWIA, magnetic field strength B_1 above the arc was higher than B_2 below the arc, which induced that the forces acting on the upper arc column played a more important role in arc appearance. Therefore, under the action of electromagnetic force F_{e1} and plasma jet force F_{p1}, the arc extended vertically downward, freely stretching. Additionally, in this experimental condition, necking phenomenon appeared at the tip of the wire, and a slender liquid column was generated (Fig. 3(c, f)), which was a typical feature of streaming spray transfer. The liquid column was apparently thinner than the welding wire, with a 0.79 mm droplet diameter and a 666.7 Hz transfer frequency. Moreover, the droplet transfer path was relatively regular, almost vertical downward. As shown in Fig. 4(c, d), because of the special electrode arrangement of TTWIA, the forces acting on droplet mainly included gravity F_g, surface tension F_σ, electromagnetic force F_{em}, and arc pressure F_a, in which F_a was not contained in traditional GMAW [20]. The resultant force promoting droplet detachment was greater than the resultant force hindering the droplet detachment, namely $F_g + F_{em} + F_a > F_\sigma$, once process parameters were selected appropriately.

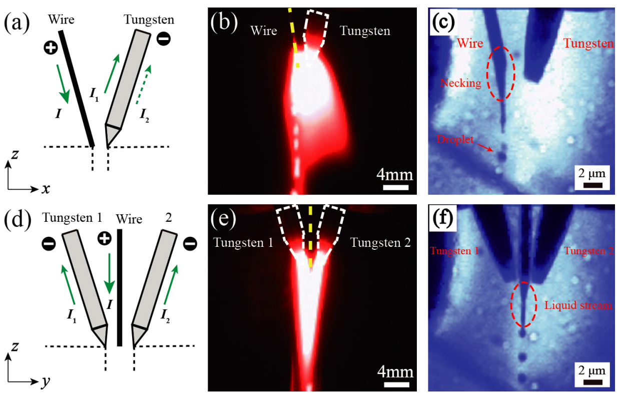

Fig. 3. Typical arc appearance and droplet transfer process of TTWIA in different directions, (a, d) Electrode structure; (b, e) Arc shape; (c, f) Droplet transfer.

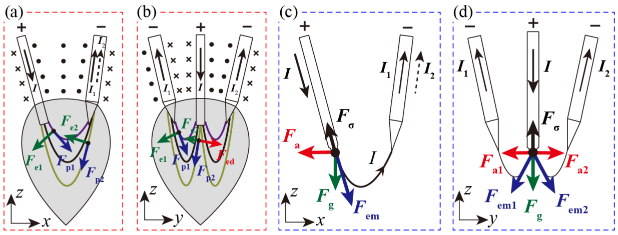

Fig. 4. Force analysis on (a, b) charged particles in arc plasma and (c, d) droplet of TTWIA.

3.2. Thin-walled part

Fig. 5 shows the multi-layer single-bead formed part deposited by TTWIA. The arc current and the deposition velocity were separately set to 200 A and 5 mm/s, and 10 layers were deposited using a unidirectional wire-leading deposition method. Moreover, the wire feeding velocity was set to 6.75 m/min, selected to achieve optimal arc stability [15]. The component fabricated by TTWIA demonstrated excellent forming quality, featuring high surface smoothness and optimal interlayer bonding without evident defects (Fig. 5(a, b)). Under the same experimental conditions, the wire feeding speed of TIG was set at 1.80 m/min, as it was the maximum allowable wire feeding speed for achieving well-formed deposited layer. Notably, this value was also close to those reported by Pattanayak et al. [21] and Zahidin et al. [22]. Consequently, under the present experimental conditions, the wire deposition rate of TIG could achieve 0.96 kg/h, while the wire deposition rate of TTWIA could reach 3.60 kg/h, representing a more than 2.75-fold increase compared to that of conventional TIG.

Fig. 5(c, d) display the cross section appearance of the thin-walled parts fabricated by TTWIA and TIG under identical experimental conditions, and the contours are extracted in Fig. 5(e, f). The effective height and area of the thin-walled part fabricated by TIG were 8.6 mm and 55.0 mm^2 separately, while the effective height and area of the thin-walled part fabricated by TTWIA were 25.3 mm and 159.4 mm^2 respectively, indicating a 1.9-fold increase in forming efficiency was achieved compared with that deposited by TIG. Besides, the area of substrate heat-affected zone (HAZ) produced by TTWIA was only 6.1 mm^2, which was 53.8% less than that of TIG.

For WAAM process, the surface of the deposited component is rough and uneven, with certain variations in both the width and height of the deposited layers. Surface roughness Ra and material utilization rate ξ are separately defined in order to precisely evaluate the formation accuracy of the fabricated component [16]. Generally, a smaller R_a value indicates higher geometric accuracy of the fabricated component, while ξ exhibits the opposite trend.

As shown in Fig. 5(g), under these experimental conditions, the R_a and ξ of the thin-walled part fabricated by TTWIA were 1.21 mm and 83.74%, respectively. In comparison, the corresponding values of the deposited component fabricated by traditional TIG were 0.51 mm and 90.98%, separately. Therefore, the formation accuracy of the deposited wall fabricated by TTWIA was slightly inferior to that of conventional TIG.

Fig. 6 shows the electrical signals during the deposition processes. The fluctuation amplitude of arc voltage served as a more representative indicator of the process stability, owing to the drooping-characteristic power source employed in this experiment. Based on statistical principles, the arc voltage variation coefficient η [13] could be used to quantitatively characterize the fluctuation of arc voltage. Generally, a smaller η indicated a higher process

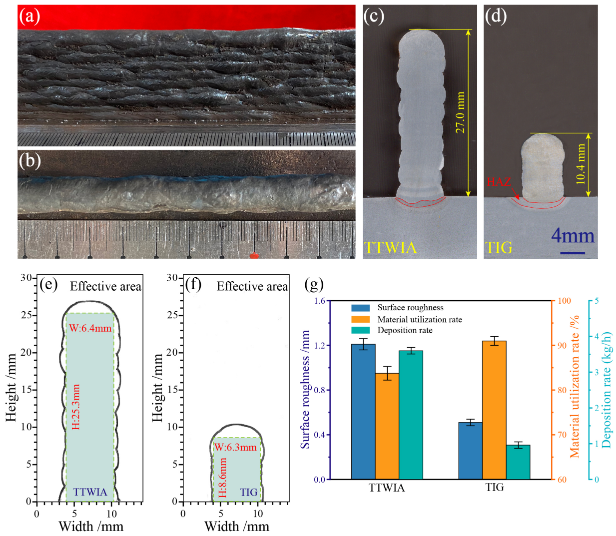

Fig. 5. Forming appearance and cross sections of the thin-walled part, (a) Front view deposited by TTWIA; (b) Top view deposited by TTWIA; (c, e) TTWIA; (d, f) TIG; (g) Statistical forming parameters.

stability. In conventional TIG deposition process, the arc voltage fluctuation was small (Fig. 6(a)), with a low η of approximately 4.5%, attributed to the inherent stability and minimal spatter characteristic of TIG. TTWIA deposition process similarly demonstrated minor arc voltage fluctuation (Fig. 6(b)), with a η of merely 4.3%, which indicated that TTWIA deposition process maintained the high stability of conventional TIG deposition process.

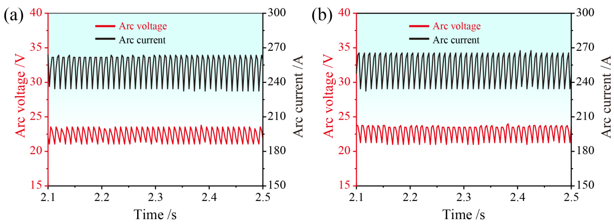

Fig. 6. Electrical signals during deposition process, (a) TIG; (b) TTWIA.

3.3. Microstructure and property

During the multi-layer single-bead deposition process, the microstructure of the deposited component presented inhomogeneity because of varying heating histories and cooling conditions experienced by the deposited metal at different heights. The microstructure of the formed part was observed in four regions along the height direction: the bottom, lower-middle, upper-middle, and top sections.

Fig. 7 shows the microstructure of different regions in the formed component fabricated by TTWIA. The bottom region of the formed component exhibited columnar grains, primarily composed of upper bainite and ferrite (Fig. 7(a)). This was primarily due to the fact that the bottom of the thin-walled part was close to the substrate, which provided better heat dissipation conditions, resulting in directional solidification of the molten pool. Besides, the microstructures of the upper-middle and lower-middle regions in the formed component showed minimal differences, with both consisting of fine equiaxed grains predominantly comprising pearlite and ferrite (Fig. 7(b, c)). The middle layers were subjected to preheating from preceding layers and post-heating from subsequent layers. This process was equivalent to normalizing by the next deposited layer, thereby promoting microstructural refinement. Additionally, the top region of the deposited component featured coarse columnar grains, mainly consisting of upper bainite,

lower bainite and ferrite (Fig. 7(d)). This was closely related to the poor heat dissipation conditions and slower cooling rate of the top deposited layer, as well as the fact that the top layer did not undergo post-heating from subsequent layers.

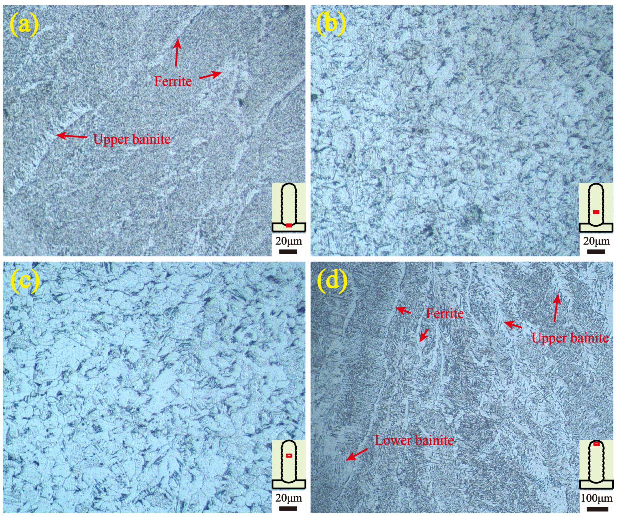

Fig. 7. Microstructures of the thin-walled part deposited by TTWIA, (a) Bottom; (b) Middle lower; (c) Middle upper; (d) Top.

Fig. 8(a) displays the microhardness variation of the deposited wall fabricated by TTWIA, in which microhardness was measured sequentially from bottom to top on the cross section of the deposited wall with a spacing of 1 mm. For the deposited part above the substrate, the microhardness first decreased and then increased from the bottom up, with a maximum hardness (217.7 HV) adjacent to the substrate remelting zone. Upper bainite precipitated in the microstructure near the bottom region, as well as the top region of the thin-walled part, thereby enhancing its hardness. In contrast, the intermediate layers predominantly consisted of ferrite and pearlite in the microstructure, resulting in comparatively lower microhardness.

The tensile strength and elongation of the original wire (AWS ER70S-6) used in this experiment are ≥ 500 MPa and ≥ 22%, respectively [23]. Fig. 8(b) displays the tensile properties of the formed part fabricated by TTWIA. The tensile strength of the formed part approached that of the original wire, as well as its elongation. It suggested that the deposited component fabricated by TTWIA possessed satisfactory mechanical properties. Besides, the formed part exhibited higher tensile strength along the deposited direction (535.5 MPa) than in the perpendicular direction (491.5 MPa), while presenting lower elongation (25.0%) along the deposited direction than in the perpendicular direction (35.0%). It indicated that the formed part fabricated by TTWIA possessed significant anisotropy in their mechanical properties. Moreover, for the forming components all made of the same welding wire ER70S-6, the tensile strength obtained by TTWIA additive manufacturing was higher than that obtained by GMAW additive manufacturing (480 MPa) [24] and CMT additive manufacturing (402 MPa) [25].

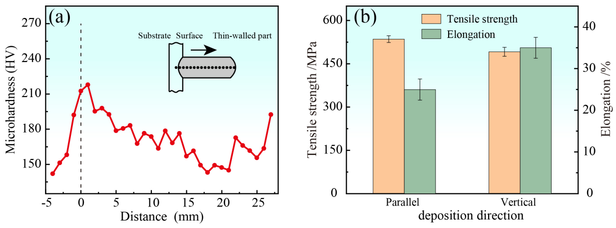

Fig. 8. Mechanical property of the deposited wall fabricated via TTWIA, (a) Microhardness distribution; (b) Tensile strength.

3.4. Molten pool temperature field

According to the Stefan-Boltzmann principle, the temperature distribution of the molten metal could be measured via an infrared camera [26, 27], in which the emissivity on the molten pool surface ought to be attained primarily. A calibration experiment of the emissivity has been carried out in this study, and the experimental method was same as reference [15]. To avert the interfere of the arc light, the molten metal temperature was collected in the manner of the arc instantaneous quenching. Fig. 9(a, b) shows the collected molten metal temperature fields of TTWIA and conventional TIG within 1.0 s when the arc was burnt out. Based on the distribution characteristic of the measured temperature, taking 773 K as the boundary, the temperature field of the molten metal could be separated into two zones, namely high-temperature zone and low-temperature zone.

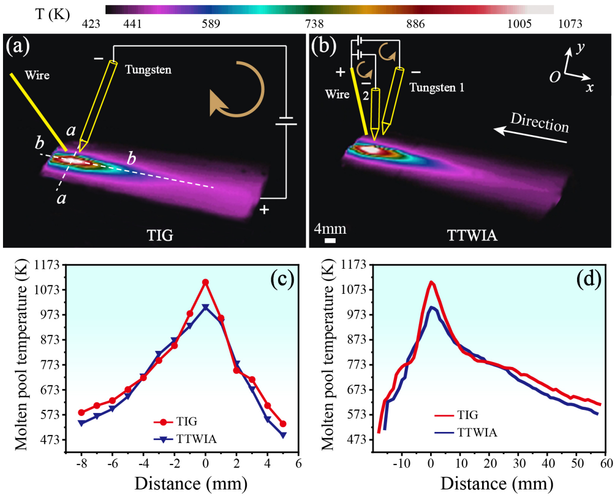

Fig. 9. Molten pool temperature distribution, (a) TIG; (b) TTWIA; (c) Temperatures on line a-a; (d) Temperatures on line b-b.

Moreover, to analyze the temperature variation of the molten pool quantificationally, the temperatures on line a-a and b-b were obtained, namely perpendicular to and located in the symmetry position of the deposited layer (Fig. 9(c, d)). The conventional TIG deposition process exhibited a higher molten pool temperature, with its peak temperature reaching 1103.5 K. The high-temperature area was relatively small, measuring a width of 5.1 mm and a length of 29.0 mm. In contrast, TTWIA deposition process demonstrated a lower molten pool temperature, with a peak temperature of approximately 1002.5 K, but featured a slightly larger high-temperature area measuring a width of 5.5 mm and a length of 30.0 mm. This phenomenon was intimately relevant to the thermal transfer characteristics of TTWIA and conventional TIG.

3.5. Heat transfer behavior

3.5.1. Substrate heat input

In the conventional TIG deposition process, the substrate served as the anode. The primary heat input to the substrate was achieved through thermal transfer via collisions between high-velocity charged particles in the arc plasma and the substrate surface, along with radiation and thermal conduction from the high-temperature plasma. Thus, the thermal transmission process in anode zone exhibits considerable complexity. Fig. 10(a) shows a schematic diagram of energy transfer in the anode zone during conventional TIG deposition process. According to the law of energy conservation, the heat input to the substrate (Q_T) could be expressed as [20]:

$$Q_T = \frac{j^2}{\sigma} + \nabla \cdot \left(\frac{k}{c_p} \nabla h \right) + S + S_d \tag{1}$$

where σ, k, c_p, and h are the electrical conductivity, thermal conductivity, specific heat, and enthalpy, respectively. On the right side of the above formula, the first term represents the resistive heat generated in the substrate, the second term corresponds to the thermal conduction from the arc column, the third source term (S) accounts for the heat production in anode sheath region, and the fourth source term (S_d) denotes the heat in droplets.

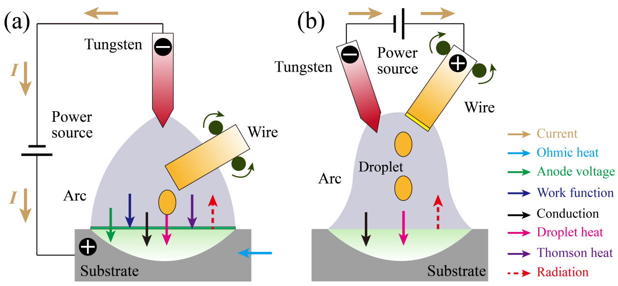

Fig. 10. Schematic diagram of heat transfer in substrate, (a) TIG; (b) TTWIA.

In the case of TTWIA deposition process, the substrate no longer served as an electrode of arc plasma. Consequently, the energy transmitted to the substrate did not include the heat production in electrode zone and the resistive heating produced in substrate. Instead, it primarily originated from the thermal conduction of high-temperature arc column and the heat in droplets, as displayed in Fig. 10(b). Therefore, the energy transmitted into the substrate (Q_I) could be expressed as [28]:

$$Q_I = \nabla \cdot \left(\frac{k}{c_p} \nabla h \right) - \varepsilon a T_b^4 - q_{ev} H_{ev} + S_d \tag{2}$$

where T_b is the substrate temperature, $\varepsilon a T_b^4$ denotes the radiative heat loss from the substrate to ambient environment, $q_{ev} H_{ev}$ indicates the evaporative heat loss from the substrate.

Based on the above analysis, compared with conventional TIG deposition process, the heat input to the substrate in TTWIA deposition process could not include the heat production in electrode zone and the resistive heating. In arc deposition process, the heat production in electrode zone played a decisive role in heating and melting both the electrode and substrate. Specifically, the heat production in the arc electrode zone constituted the primary source of the heat input to the substrate, which was significantly higher than other forms of energy transfer [29]. Therefore, this special energy transfer mode of TTWIA also determined its characteristic of low heat input, thus leading to a smaller peak temperature in molten metal.

3.5.2. Wire melting heat

For conventional TIG deposition process, the melting of welding wire primarily depended on absorbing heat from high-temperature arc plasma, as illustrated in Fig. 11(a). Thus, the heat employed to melt the welding wire (Q_{wT}) could be expressed as [30]:

$$Q_{\mathrm{wT}} = \nabla \cdot \left(\frac{k}{c_{\mathrm{p}}} \nabla h \right) - \rho_{\mathrm{d}} f_{\mathrm{d}} h_{\mathrm{d}} \tag{3}$$

where $\rho_{\mathrm{d}} f_{\mathrm{d}} h_{\mathrm{d}}$ denotes the heat lost due to the detachment of the droplets.

However, for TTWIA deposition process, the wire served as the positive pole of the arc. The heat required to melt welding wire primarily came from heat production in electrode region of the arc, supplemented by a small amount of resistive heat from the wire and heat conduction from the high-temperature arc, as illustrated in Fig. 11(b). Specifically, the wire melting heat Q_{wI} could be expressed as [30]:

$$Q_{\mathrm{wI}} = \frac{j^2}{\sigma} + \nabla \cdot \left(\frac{k}{c_{\mathrm{p}}} \nabla h \right) + S - \rho_{\mathrm{d}} f_{\mathrm{d}} h_{\mathrm{d}} \tag{4}$$

Therefore, compared with conventional TIG, the wire melting mechanism of TTWIA underwent fundamental changes. The heat generated in the electrode region ensured a higher wire melting rates, thereby realizing a high-deposition-rate additive manufacturing process. Consequently, this process featured an enlarged high-temperature region in molten metal.

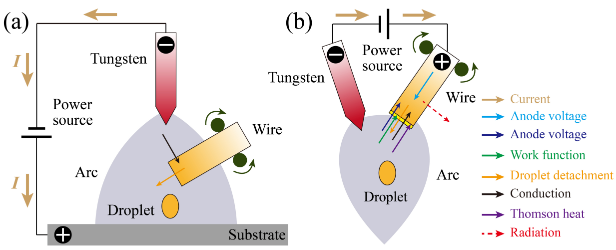

Fig. 11. Schematic diagram of heat transfer in wire, (a) TIG; (b) TTWIA.

4. Conclusions

1. Under identical experimental conditions, the wire deposition rate of TTWIA was over 2.75 times higher than that of TIG. Moreover, TTWIA deposition process maintained the high stability of conventional TIG deposition process. Besides, the surface roughness and material utilization rate of the component fabricated by TTWIA were 1.21 mm and 83.74%, respectively.
2. The bottom and top of the component fabricated by TTWIA featured coarse columnar grains, while the middle region showed fine equiaxed grains. Besides, the microhardness of the component first decreased and then increased from the bottom to the top. Additionally, the tensile strength of the component was higher than that fabricated by GMAW and CMT additive manufacturing using the same ER70S-6 wire.
3. Compared with TIG deposition process, the heat input to the substrate in TTWIA deposition process could not include the heat production in the electrode region and the resistive heat, resulting in a lower molten pool temperature. Furthermore, the heat production in the electrode region ensured a higher wire melting rates, thereby realizing a high-deposition-rate additive manufacturing process.

Acknowledgements

This work was supported by Shandong Provincial Natural Science Foundation (ZR2024QE323), and Key R&D Program of Shandong Province, China (Initiative for Enhancing the Innovation Capability of Technology-based SMEs) (2025TSGCCZZB0408).

References

[1] S. Gain and D. Veeman, (2025) *"A review on advances and challenges in wire arc additive manufacturing: Process parameters, microstructural evolution and material performance across alloys"* **Journal of Alloys and Compounds *1029***: 180735. DOI: 10.1016/j.jallcom.2025.180735.

[2] Y. H. Kim, D. R. Gunasegaram, P. W. Cleary, and A. B. Murphy, (2025) *"Numerical modelling of wire arc additive manufacturing: methods, status, trends, and opportunities"* **Journal of Physics D: Applied Physics *58***: 143001. DOI: 10.1088/1361-6463/adb3b0.

[3] Q. Han, X. Li, M. Dong, and G. Zhang, (2021) *"Enhanced curve-fitting model of the bead section profile and the corresponding overlapping model for twin-electrode gas tungsten arc–based additive manufacturing"* **International Journal of Advanced Manufacturing Technology *116***: 1151–1167. DOI: 10.1007/s00170-021-07501-9.

[4] M. B. Schwedersky, Á. F. d. Rosa, M. d. A. Souza, and R. H. G. e. Silva, (2025) *"Arc characteristic of multi-cathode three-electrode GTAW (TE-GTAW)"* **Welding in the World *69***: 2609–2617. DOI: 10.1007/s40194-024-01887-2.

[5] Z. Zeng, Z. Zhang, X. Jin, H. Huang, L. Zhang, and J. Zhang, (2025) *"Microstructure evolution and properties of Inconel 625 alloy fabricated by hot-wire TIG additive manufacturing"* **Journal of Alloys and Compounds *1032***: 181113. DOI: 10.1016/j.jallcom.2025.181113.

[6] T. Zhang, L. Wang, C. Xu, J. Cheng, and K. Wang, (2023) *"Early-warning system for copper alloy abnormal molten pool in wire-arc additive manufacturing via convolutional neural network method"* **Journal of Materials Engineering and Performance *32***: 11230–11239. DOI: 10.1007/s11665-023-07949-8.

[7] S.-C. Park, H.-S. Bang, and W.-J. Seong, (2020) *"Effects of material properties on angular distortion in wire arc additive manufacturing: experimental and computational analyses"* **Materials *13***: 1399. DOI: 10.3390/ma13061399.

[8] X. Zhang, F. Martina, J. Ding, X. Wang, and S. W. Williams, (2017) *"Fracture toughness and fatigue crack growth rate properties in wire + arc additive manufactured Ti-6Al-4V"* **Fatigue & Fracture of Engineering Materials & Structures *40***: 790–803. DOI: 10.1111/ffe.12547.

[9] F. Wang, S. Williams, and M. Rush, (2011) *"Morphology investigation on direct current pulsed gas tungsten arc welded additive layer manufactured Ti6Al4V alloy"* **International Journal of Advanced Manufacturing Technology *57***: 597–603. DOI: 10.1007/s00170-011-3299-1.

[10] T. Hauser, R. T. Reisch, P. P. Breese, B. S. Lutz, M. Pantano, Y. Nalam, K. Bela, T. Kamps, J. Volpp, and A. F. H. Kaplan, (2021) *"Porosity in wire arc additive manufacturing of aluminium alloys"* **Additive Manufacturing *41***: 101993. DOI: 10.1016/j.addma.2021.101993.

[11] J. Wang, D. Wu, P. Liao, C. Y. Tian, M. Q. Li, and J. C. Feng, (2013) *"Metal transfer and arc behaviour of novel consumable and non-consumable electrode indirect arc droplet welding"* **Science and technology of welding and joining *18***: 261–270. DOI: 10.1179/1362171812Y.0000000103.

[12] T. A. Rodrigues, V. R. Duarte, R. M. Miranda, T. G. Santos, and J. P. Oliveira, (2021) *"Ultracold-wire and arc additive manufacturing (UC-WAAM)"* **Journal of Materials Processing Technology *296***: 117196. DOI: 10.1016/j.jmatprotec.2021.117196.

[13] Y. Zhu, Z. Wang, R. Liu, and L. Liu, (2022) *"Study on arc behavior and droplet transfer in twin-electrode TIG-MIG indirect arc welding"* **International Journal of Advanced Manufacturing Technology *120***: 6821–6831. DOI: 10.1007/s00170-022-09131-1.

[14] Y. Zhu, R. Liu, and L. Liu, (2023) *"A comparison of single and twin tungsten electrode – wire electrode IAW"* **Materials and manufacturing processes *38***: 1436–1444. DOI: 10.1080/10426914.2022.2146715.

[15] Y. Zhu, Z. Zhou, C. Liu, P. Li, H. Fang, Q. Yang, and J. Lu, (2025) *"Research on deposition forming of two tungsten electrode – wire electrode indirect arc welding"* **Journal of Materials Engineering**: DOI: 10.11868/j.issn.1001-4381.2025.000295.

[16] Y. Zhu, S. Gao, S. Yu, and D. Ma, (2025) *"Forming characteristic analysis in twin tungsten electrode – Wire electrode indirect arc based additive manufacturing"* **Vacuum *232***: 113902. DOI: 10.1016/j.vacuum.2024.113902.

[17] Y. Zhu, H. He, D. Ma, H. Liu, P. Li, and L. Zhang, (2026) *"Influences of process parameters on twin tungsten electrode – wire electrode indirect arc additive manufacturing process"* **Journal of Applied Science and Engineering *32***: 26032040. DOI: 10.6180/jase.202609_32.040.

[18] C. Jing, Z. Chen, B. Liu, T. Xu, J. Wang, T. Lu, J. Lu, Y. Guo, and C. Liu, (2022) *"Improving mechanical strength and isotropy for wire-arc additive manufactured 304L stainless steels via controlling arc heat input"* **Materials Science & Engineering A *845***: 143223. DOI: 10.1016/j.msea.2022.143223.

[19] L. Wang, J. Xue, and Q. Wang, (2019) *"Correlation between arc mode, microstructure, and mechanical properties during wire arc additive manufacturing of 316L stainless steel"* **Materials Science & Engineering A *751***: 183–190. DOI: 10.1016/j.msea.2019.02.078.

[20] W. Ou, W. Zhao, G. Guo, J. Dai, and L. Fan, (2025) *"Wire-droplet-substrate integrated model for heat transfer and deposition geometry prediction in GMAW-based wire arc additive manufacturing"* **Welding in the World *69***: 2941–2959. DOI: 10.1007/s40194-025-01931-9.

[21] S. Pattanayak and S. K. Sahoo, (2021) *"Gas metal arc welding based additive manufacturing—a review"* **CIRP Journal of Manufacturing Science and Technology** ***33***: 398–442. DOI: 10.1016/j.cirpj.2021.04.010.

[22] M. R. Zahidin, F. Yusof, S. H. A. Rashid, S. Mansor, S. Raja, M. F. Jamaludin, Y. H. Manurung, M. S. Adenan, and N. I. S. Hussein, (2023) *"Research challenges, quality control and monitoring strategy for wire arc additive manufacturing"* **Journal of Materials Research and Technology** ***24***: 2769–2794. DOI: 10.1016/j.jmrt.2023.03.200.

[23] X. Ba, S. Su, Y. Li, and L. Liu, (2025) *"Effect of current process on BCTW-GIA additive manufacturing"* **Materials and Manufacturing Processes** ***40***: 1535–1545. DOI: 10.1080/10426914.2025.2522051.

[24] C. Ma, Y. Liu, C. Li, H. Dong, D. Li, X. Wu, P. Liu, Q. Sun, H. Jin, and F. Zhang, (2020) *"Mechanical properties of carbon steel by compound arc and vibration shock forging-rolling"* **Journal of Manufacturing Processes** ***60***: 11–22. DOI: 10.1016/j.jmapro.2020.10.005.

[25] P. Dirisu, G. Supriyo, F. Martina, X. Xu, and S. Williams, (2020) *"Wire plus arc additive manufactured functional steel surfaces enhanced by rolling"* **International Journal of Fatigue** ***130***: 105237. DOI: 10.1016/j.ijfatigue.2019.105237.

[26] D. Yang, G. Wang, and G. Zhang, (2017) *"Thermal Analysis for Single-Pass Multi-Layer GMAW Based Additive Manufacturing Using Infrared Thermography"* **Journal of Materials Processing Technology** ***244***: 215–224. DOI: 10.1016/j.jmatprotec.2017.01.024.

[27] G. R. Peacock, (2000) *"Thermal imaging of liquid steel and slag in a pouring stream"* **Proceedings of SPIE** ***4020***: 50–60. DOI: 10.1117/12.381579.

[28] R. T. C. Choo, J. Szekely, and R. C. Westhoff, (1992) *"On the calculation of the free surface temperature of gas-tungsten-arc weld pools from first principles: Part I. modeling the welding arc"* **Metallurgical and Materials Transactions B** ***23B***: 357–369. DOI: 10.1007/BF02656291.

[29] V. M. J. Varghese, M. R. Suresh, and D. S. Kumar, (2013) *"Recent developments in modeling of heat transfer during TIG welding – a review"* **International Journal of Advanced Manufacturing Technology** ***64***: 749–754. DOI: 10.1007/s00170-012-4048-9.

[30] J. Hu and H. L. Tsai, (2007) *"Heat and mass transfer in gas metal arc welding. Part I: The arc"* **International Journal of Heat and Mass Transfer** ***50***: 833–846. DOI: 10.1016/j.ijheatmasstransfer.2006.08.025.